HHS Public Access

Author manuscript

Radiology. Author manuscript; available in PMC 2020 September 01.

Published in final edited form as:

Radiology. 2020 September ; 296(3): 575–583. doi:10.1148/radiol.2020200373.

Molecular MRI of the Immuno-Metabolic Interplay in a Rabbit Liver Tumor Model:

A Biomarker for Resistance Mechanisms in Tumor-targeted Therapy?

Lynn Jeanette Savic, MD, **Luzie A. Doemel, BSc**, **Isabel Theresa Schobert, MD**, **Ruth Rebecca Montgomery, PhD**, **Nikhil Joshi, PhD**, **John James Walsh, BSc**, **Jessica Santana, MSc**, **Vasily Pekurovsky, BSc**, **Xuchen Zhang, MD**, **MingDe Lin, PhD**, **Lucas Adam, MD**, **Annemarie Boustani, MD**, **James Duncan, PhD**, **Lin Leng, PhD**, **Richard John Bucala, MD, PhD**, **S. Nahum Goldberg, MD**, **Fahmeed Hyder, PhD**, **Daniel Coman, PhD**, **Julius Chapiro, MD**

Department of Radiology and Biomedical Imaging (L.J.S., L.A.D., I.T.S., J.J.W., J.S., M.D.L., L.A., A.B., J.D., F.H., D.C., J.C.), Department of Internal Medicine, Section of Rheumatology (R.R.M., L.L., R.J.B.), Department of Immunobiology (N.J.), and Department of Pathology (V.P., X.Z.), Yale University School of Medicine, 300 Cedar St, New Haven, CT 06520; Institute of Radiology, Charité-Universitätsmedizin Berlin, corporate member of Freie Universität Berlin, Humboldt-Universität, and Berlin Institute of Health, Berlin, Germany (L.J.S., L.A.D., I.T.S., L.A.); Visage Imaging, San Diego, Calif (M.D.L.); Department of Biomedical Engineering, Yale School of Engineering and Applied Science, New Haven, Conn (J.D.); and Department of Radiology, Hadassah Hebrew University Medical Center, Jerusalem, Israel (S.N.G.).

Address correspondence to J.C. (j.chapiro@googlemail.com).

Author contributions: Guarantors of integrity of entire study, L.J.S., N.J., X.Z., L.A., F.H., J.C.; study concepts/study design or data acquisition or data analysis/interpretation, all authors; manuscript drafting or manuscript revision for important intellectual content, all authors; approval of final version of submitted manuscript, all authors; agrees to ensure any questions related to the work are appropriately resolved, all authors; literature research, L.J.S., L.A.D., I.T.S,. R.R.M., A.B., L.L., S.N.G., F.H., D.C., J.C.; clinical studies, V.P., X.Z.; experimental studies, L.J.S., L.A.D., I.T.S,. R.R.M., J.J.W., J.S., X.Z., M.D.L., L.A., J.D., L.L., R.J.B., F.H., D.C., J.C.; statistical analysis, L.J.S., J.D., S.N.G., F.H., J.C.; and manuscript editing, all authors

Online supplemental material is available for this article.

Disclosures of Conflicts of Interest: L.J.S. Activities related to the present article: disclosed no relevant relationships. Activities not related to the present article: disclosed no relevant relationships. Other relationships: was a Leopoldina Postdoc Fellow during the conduct of this study and received grants from the Rolf W. Günther Foundation for Radiological Science outside of the submitted work; is a participant in the BIH-Charité Junior Clinician Scientist Program funded by the Charité–Universiätsmedizin Berlin and the Berlin Institute of Health. **L.A.D.** Activities related to the present article: disclosed no relevant relationships. Activities not related to the present article: was employed by Yale University as a postgraduate associate during research work for this project. Other relationships: disclosed no relevant relationships. **I.T.S.** Activities related to the present article: disclosed no relevant relationships. Activities not related to the present article: received grants from the Biomedical Education Program (BMEP) during research work for this project. Other relationships: disclosed no relevant relationships. **R.R.M.** disclosed no relevant relationships. **N.J.** disclosed no relevant relationships. **J.J.W.** disclosed no relevant relationships. **J.S.** disclosed no relevant relationships. **V.P.** disclosed no relevant relationships. **X.Z.** disclosed no relevant relationships. **M.L.** Activities related to the present article: is an employee of Visage Imaging. Activities not related to the present article: disclosed no relevant relationships. Other relationships: disclosed no relevant relationships. **L.A.** disclosed no relevant relationships. **A.B.** disclosed no relevant relationships. **J.D.** disclosed no relevant relationships. **L.L.** disclosed no relevant relationships. **R.J.B.** disclosed no relevant relationships. **S.N.G.** Activities related to the present article: disclosed no relevant relationships. Activities not related to the present article: is a paid consultant for Cosman instruments and Angiodynamics. Other relationships: disclosed no relevant relationships. **F.H.** disclosed no relevant relationships. **D.C.** disclosed no relevant relationships. **J.C.** Activities related to the present article: disclosed no relevant relationships. Activities not related to the present article: is a paid consultant for Guerbet and Philips Healthcare; institution has grants/grants pending from Guerbet, Philips, and Boston Scientific. Other relationships: disclosed no relevant relationships.

Abstract

Background: The immuno-metabolic interplay has gained interest for determining and targeting immunosuppressive tumor micro-environments that remain a barrier to current immuno-oncologic therapies in hepatocellular carcinoma.

Purpose: To develop molecular MRI tools to reveal resistance mechanisms to immuno-oncologic therapies caused by the immuno-metabolic interplay in a translational liver cancer model.

Materials and Methods: A total of 21 VX2 liver tumor–bearing New Zealand white rabbits were used between October 2018 and February 2020. Rabbits were divided into three groups. Group A ($n = 3$) underwent intra-arterial infusion of gadolinium 160 (^{160}Gd)–labeled anti–human leukocyte antigen–DR isotope (HLA-DR) antibodies to detect antigen-presenting immune cells. Group B ($n = 3$) received rhodamine-conjugated superparamagnetic iron oxide nanoparticles (SPIONs) intravenously to detect macrophages. These six rabbits underwent 3-T MRI, including T1- and T2-weighted imaging, before and 24 hours after contrast material administration. Group C ($n = 15$) underwent extracellular pH mapping with use of MR spectroscopy. Of those 15 rabbits, six underwent conventional transarterial chemoembolization (TACE), four underwent conventional TACE with extracellular pH– buffering bicarbonate, and five served as untreated controls. MRI signal intensity distribution was validated by using immunohistochemistry staining of HLA-DR and CD11b, Prussian blue iron staining, fluorescence microscopy of rhodamine, and imaging mass cytometry (IMC) of gadolinium. Statistical analysis included Mann-Whitney *U* and Kruskal-Wallis tests.

Results: T1-weighted MRI with ^{160}Gd-labeled antibodies revealed localized peritumoral ring enhancement, which corresponded to gadolinium distribution detected with IMC. T2-weighted MRI with SPIONs showed curvilinear signal intensity representing selective peritumoral deposition in macrophages. Extracellular pH–specific MR spectroscopy of untreated liver tumors showed acidosis (mean extracellular pH, 6.78 ± 0.09) compared with liver parenchyma (mean extracellular pH, 7.18 ± 0.03) ($P = .008$) and peritumoral immune cell exclusion. Normalization of tumor extracellular pH (mean, 6.96 ± 0.05; $P = .02$) using bicarbonate during TACE increased peri- and intratumoral immune cell infiltration ($P = .002$).

Conclusion: MRI in a rabbit liver tumor model was used to visualize resistance mechanisms mediated by the immuno-metabolic interplay that inform susceptibility and response to immuno-oncologic therapies, providing a therapeutic strategy to restore immune permissiveness in liver cancer.

Summary

Noninvasive molecular MRI can be used to visualize resistance mechanisms mediated by the tumor metabolism and immune evasion for strategic targeting by local-regional and immunotherapy in liver cancer.

Hepatocellular carcinoma (HCC) is the third most common cause of cancer-related deaths worldwide (1). The vast majority of patients are diagnosed at disease stages no longer amenable to curative therapies. In this setting, intra-arterial therapies such as conventional oil-based transarterial chemoembolization (TACE) are widely applied and approved by guidelines (2). Conversely, established conventional systemic therapies have failed to elicit

meaningful survival benefits (3). This negative trend has been recently challenged by the emerging concept of immunotherapies (4). Immunomodulatory checkpoint inhibitors are thought to facilitate immune cell infiltration, thus enabling the resources of the patient's own immune system to elicit a potent response against the tumor (4). However, clinical trials using checkpoint inhibitors in liver cancer (Check-Mate-040 and CheckMate-459) demonstrated sustained tumor response of only 20%, while 80% of participants failed to respond (4,5). Although a variety of resistance mechanisms are under investigation to explain the failure of these therapies, the immuno-metabolic interplay as an organizing principle of immune evasion has gained interest (6–9). One such factor postulated is the profound extracellular acidosis driven by hyperglycolytic tumor metabolism ("Warburg effect"), which contributes to immune cell exhaustion and quiescence of local immune defense (9,10). Hypoxia further drives the hyperglycolytic phenotype of cancer cells and consecutive accumulation of lactate and protons, leading to low extracellular pH and direct T-cell suppression in the tumor micro-environment (11).

The commonly cited principle behind combining TACE with immunotherapies proposes to exploit tumor-associated antigens that are exposed during tissue destruction and presented by anti-gen-presenting immune cells (APCs) to activate T-lymphocytes (12). The key feature of typical APCs, such as dendritic cells, macrophages, and B-lymphocytes, is the constitutive expression of major histocompatibility II molecules, such as the human leukocyte antigen–DR isotope (HLA-DR) (13). In addition, recent investigations revealed the potency of conventional TACE to reverse tumor-characteristic extracellular acidosis in and surrounding the tumor toward a normalized extracellular pH (14). Yet, conventional TACE is also known to induce ischemia while blocking lactate removal from the tumor micro-environment. This may further deregulate the disrupted metabolic phenotype of HCC (11,15).

There is an unmet clinical need to design imaging tools capable of phenotyping the immuno-metabolic interplay to reveal and target underlying mechanisms of immune resistance to restore immune permissiveness (9). Our study therefore aimed at developing such molecular MRI tools to reveal and target tumor micro-environment components of the immuno-metabolic interplay that may cause resistance to immunotherapy using a translational rabbit liver tumor model for conventional TACE.

Materials and Methods

VX2 Rabbit Liver Tumor Model

Male New Zealand white rabbits (Charles River Laboratories, Boston, Mass; age, 11–17 weeks; weight, 2.5–4 kg) were used under approved animal care and use committee protocols as described previously (14,16). Briefly, VX2 tumor chunks were injected into the left rabbit liver by means of median laparotomy and allowed to grow for 14 days until a well-delineated tumor (1.0–2.0 cm in diameter) was measurable at MRI (L.J.S., with 6 years of experience; I.T.S., with 2 years of experience; L.A.D., with 1 year of experience in animal experiments).

Experimental Study Design

A total of 21 tumor-bearing animals were included in our pilot study. Prior to tumor implantation, the animals were randomly assigned to one of the following groups. Group A (n = 3) underwent intra-arterial infusion of gadolinium 160 (^{160}Gd)–labeled anti–HLA-DR antibodies to detect APCs. Group B (n = 3) received intravenous administration of rhodamine-conjugated superparamagnetic iron oxide nanoparticles (SPIONs) to detect macrophages. These six rabbits underwent 3-T MRI before and 24 hours after contrast material administration (Fig 1). Group C (n = 15) underwent extracellular pH mapping with MR spectroscopy (14,17). Of those 15 rabbits, six underwent conventional TACE and four received a combination of acid-neutralizing intra-arterial bicarbonate with subsequent conventional TACE to prevent washout of bicarbonate to consolidate its extracellular pH–buffering effect. Another five rabbits served as untreated controls. MRI signal intensity distribution was validated ex vivo by using immunofluorescence, immuno-histochemistry, and imaging mass cytometry (IMC).

Group A: In Vivo Imaging of APCs with ^{160}Gd-labeled Antibodies

Labeling of anti-HLA-DR antibody with ^{160}Gd.——Monoclonal antihuman HLA-DR (LN3, catalog no. 327002; BioLegend, San Diego, Calif) and fluorescein isothiocyanate-conjugated antihuman HLA-DR antibody (LN3, catalog no. ab1182; Abcam, Cambridge, England) were labeled with ^{160}Gd by using the commercially available MAXPARX8 labeling kit (Fluidigm, San Francisco, Calif) according to the manufacturer's instructions (manual PRD002v11) (18) (Appendix E1 [online]).

In vivo intra-arterial injection of ^{160}Gd-labeled antibodies.——After blunt dissection of the right common femoral artery, a 3-F vascular sheath (Cook, Bloomington, Ind) was placed and a 2-F microcatheter (JB1, Cook) was advanced into the tumor-feeding vessels, where a total of 1 mg of ^{160}Gd-labeled anti–HLA-DR antibodies mixed 1:4 with iodinated contrast material was administered under fluoroscopic guidance for 5–8 minutes. Then, the catheter was flushed with saline and contrast material deposition in the tumor evaluated on sequential cone-beam CT scans.

IMC analysis.——IMC was performed with a Hyperion imaging system coupled to a Helios mass cytometer (Fluidigm). Raw data were visualized and analyzed by using the MCD Viewer (version 1.0.560.6, Fluidigm) (18).

First, successful ^{160}Gd-labeling of the antibody was confirmed with paraffin-embedded samples from VX2 tumors stained with the ^{160}Gd-labeled fluorescein isothiocyanate–conjugated anti-HLA-DR antibody. Therefore, the distribution of fluorescein isothiocyanate fluorescence signal (wavelength, 520 nm) at immunofluorescence microscopy was compared with ^{160}Gd signal at IMC.

Second, spatial distribution of ^{160}Gd antibodies after in vivo injection was confirmed with IMC by using paraffin-embedded tissue obtained from the rabbits that had received intra-arterial administration of the antibodies. Signal intensity distribution from the ^{160}Gd antibody was evaluated in three regions (tumor, peritumoral rim, and liver), and peritumoral

rim thickness was analyzed in five random locations to compare histologic and imaging findings (19). In addition, the spleen served as a positive control for HLA-DR staining (Appendix E1 [online]).

Immunohistochemistry.——In addition to hematoxylin-eosin staining, immunohistochemistry staining of APCs was performed by using anti-HLA-DR antibody (LN-3, catalog no. ab166777, Abcam; 1:50 ratio). Histologic samples were digitalized and visualized at up to 320 magnification by using Aperio ImageScope software (version 12.3; Leica Biosystems Imaging, Vista, Calif). Peritumoral rim thickness was quantified in five random high-power fields to compare histologic to imaging findings (L.J.S., I.T.S., and L.A.D.) (19).

Group B: In Vivo Imaging of Macrophages by Using SPIONs

Intravenous SPION administration in vivo.——For in vivo imaging of macrophages, Molday ION conjugated with rhodamine B (MIRB; BioPAL, Worcester, Mass) was used as an MRI contrast reagent containing SPIONs with a colloidal size of 30 nm. Although SPIONs phagocytosed by macrophages are retained, free iron washes out over time. The agent was kept at 4°C and protected from light. Rabbits were maintained under general anesthesia, and a 22-gauge catheter was placed in the auricular vein. SPIONs at a dose of 2.5 mg/kg were diluted 1:4 with saline and infused slowly over 10–15 minutes (L.J.S.) (20).

Immunohistochemistry and immunofluorescence microscopy.——Immunohistochemistry staining of APCs and macrophages was performed by using anti–HLA-DR and anti-CD11b antibody (M1/70, catalog no. ab8878, Abcam; 1:500 in phosphate-buffered saline), respectively, and quantified as explained earlier. Prussian blue staining was conducted to detect iron and its colocalization with macrophages (21). In addition, rhodamine-conjugated SPIONs were assessed with immunofluorescence microscopy (wavelength, 561–587 nm) by using unstained paraffin-embedded tumor slides to compare signal intensity distribution to imaging findings (Appendix E1 [online]).

Group C: Extracellular pH Mapping after Conventional TACE Alone and with Bicarbonate Infusion

Conventional TACE protocol.——Conventional TACE was performed as previously reported by using doxorubicin HCl (RPI, Mount Prospect, Ill) at a concentration of 1.25 mg/mL mixed 1:2 with ethiodized oil (Lipiodol; Guerbet, Villepinte, France) followed by 0.3–0.4 mL of 100–300-mm beads (Embospheres; Merit Medical, South Jordan, Utah) until stasis (14,22).

Conventional TACE with bicarbonate protocol.——The conventional TACE protocol was modified to include intra-arterial bicarbonate infusion before embolization. First, contrast media and saline were mixed 1:1 with clinically used 4% sodium bicarbonate USP (Neut; Hospira, Lake Forest, Ill) to administer a total of 3 mL bicarbonate while advancing the catheter. From the final catheter position for embolization, 5 mL of 4% bicarbonate was infused over 5 minutes. To prevent clotting, the catheter was cleared with 2 mL saline immediately followed by conventional TACE. Angiography and conventional TACE

procedures were performed by L.J.S., who had 2 years of experience with TACE in this model.

Immunohistochemistry.——Immunohistochemistry staining of APCs was performed by using anti–HLA-DR antibody and quantified as explained earlier to compare immune cell infiltration among subgroups.

MRI Protocol

All animals underwent baseline imaging by using a human-size 3-T MRI unit (Magnetom Prisma; Siemens, Erlangen, Germany) and a 15-channel knee coil. The protocol at baseline included respiratory-gated T2-weighted spin-echo images and unenhanced and intravenous contrast material–enhanced (0.1 mmol/kg Dotarem; Guerbet, Bloomington, Ind) T1-weighted Dixon images.

Before undergoing follow-up imaging, animals received ^{160}Gd antibodies (group A), SPIONs (group B), or thulium (III)1,4,7,10-tetraazacyclododecane-1,4,7,10-tetra (TmDOTP^{52}; Macrocyclics, Plano, Tex) (group C). Apart from these experimental agents, no additional contrast media were administered at follow-up MRI. Signal intensity alterations due to^{160}Gd-conjugated antibodies were assessed on T1-weighted Dixon images (repetition time msec/echo time msec, 5.19/2.46, 3.69). SPION deposition was evaluated on respiratory-gated fat-suppressed T2-weighted spin-echo images (1000/78). The tumor masks were outlined on baseline images and overlaid onto the postcontrast MRI scans to determine the peritumoral rim. Peritumoral gadolinium (signal hyperintensity on T1-weighted images) and SPION deposition (hypointensity on T2-weighted images) were quantified by using the standard length measurement tool in RadiAnt (version 4.6.9; Medixant, Poznan, Poland) to determine the rim thickness in five random locations on the Digital Imaging and Communications in Medicine files with the largest axial tumor diameter, as previously described (19). In addition, signal intensities were measured in five random locations in the tumor, peritumoral rim, liver, and back muscle by using ImageJ software (version 1.52a; National Institutes of Health, Bethesda, Md) and signal intensity ratios were calculated (23).

Animals in group C underwent extracellular pH–specific MR spectroscopy at the follow-up MRI examination by using paramagnetic TmDOTP^{52} and biosensor imaging of redundant deviation in shifts, or BIRDS. Briefly, BIRDS data were acquired by using a three-dimensional chemical shift imaging sequence (repetition time, 8 msec). TmDOTP^{52} resonances were overlaid on T1-weighted sequences (5.2/2.5) to outline the tumor (17). Extracellular pH was assessed for 8 × 8 × 10-mm voxels inside the whole tumor and tumor edge (adjacent to tumor margin) and in the liver parenchyma from the chemical proton shifts of TmDOTP^{52} by using Matlab (version R2020a 9.8.0; Math-Works, Natick, Mass) (Appendix E1 [online]).

Statistical Analysis

Descriptive data are summarized as means 6 standard deviations, medians, and ranges. Normality testing was performed. Data sets were evaluated by using the independent nonparametric Mann-Whitney *U* or Kruskal-Wallis test to compare MRI signal intensity

ratios in groups A and B, rim thickness at MRI and histologic examination in all groups, and extracellular pH values among group C subgroups. Statistical analysis was performed with SPSS (version 24.0; IBM, Armonk, NY) and Prism (version 7.0; GraphPad, La Jolla, Calif) software by L.J.S. and D.C. A two-tailed $P < .05$ was considered indicative of a statistically significant difference.

Results

Group A: ^{160}Gd-labeled Antibodies Enable Molecular Imaging of APCs in Vivo

IMC of ^{160}Gd demonstrated signal distribution only in the peritumoral rim, which matched the spatial signal distribution of fluorescein isothiocyanate–labeled anti–HLA-DR antibodies at immunofluorescence microscopy. Immunohistochemistry analysis of anti–HLA-DR antibodies revealed immune cell infiltration in the peritumoral rim between tumor and liver tissue, with similar distribution of signal intensity to that seen at IMC and immunofluorescence microscopy (Fig E1 [online]).

For in vivo imaging of ^{160}Gd antibodies, the comparison between T1-weighted images obtained at baseline and 24 hours after injection revealed localized rim enhancement in the peritumoral zone, measuring a mean (±standard deviation) of 1.5 mm ± 0.3 in the axial plane. Before and after administration of ^{160}Gd antibodies, the liver-to-muscle ratios were 0.94 ± 0.07 and 0.75 ± 0.03, respectively ($P = .55$). After administration of ^{160}Gd antibodies, the peritumoral rim-to-muscle ratio was 0.86 ± 0.02 and the peritumoral rim-to-liver ratio was 1.17 ± 0.01. IMC of tissue harvested from these same rabbits demonstrated deposition of gadolinium only in the peritumoral rim (mean rim thickness, 1.2 mm ± 0.2), corresponding to the signal intensity distribution pattern on MRI scans, but only little signal intensity in liver parenchyma or within the actual tumor (Fig 2).

IMC of paraffin-embedded spleen 24 hours after intra-arterial delivery showed a cellular distribution pattern of ^{160}Gd signal, which confirms the specific labeling of HLA–DR–positive APCs. In addition, signal detection in the spleen was suggestive of systemic distribution of the ^{160}Gd antibodies beyond the arterially supplied target tumor to organs with high density of APCs. IMC of paraffin wax without embedded tissue (negative control) demonstrated nonspecific background signal but no cellular distribution pattern (Fig E2 [online]).

Group B: In Vivo Molecular Imaging of SPIONs Reveals Macrophage Infiltration in the Peritumoral Rim

On T2-weighted MRI scans obtained 24 hours after injection of SPIONs, a curvilinear hypointense peritumoral rim of demarcation measuring a mean of 2.1 mm ± 0.9 in the axial plane surrounded the tumor, indicating selective SPION deposition in the peritumoral rim. Mean liver-to-muscle signal intensity ratios were 1.7 ± 0.14 and 1.51 ± 0.15 before and after SPION injection, respectively ($P = .10$). After SPION injection, the mean rim-to-muscle ratio was 0.92 ± 0.12 and the mean rim-to-liver ratio was 0.61 ± 0.04.

Prussian blue staining of iron confirmed the exclusive deposition of SPION in macrophages found in this zone between the tumor and surrounding liver parenchyma (mean rim

thickness, 2.3 mm ± 0.7). By comparison, almost no Prussian blue stain was detectable within the tumor or in liver parenchyma (Fig 3).

Cellular uptake of rhodamine-conjugated SPIONs in peritumoral macrophages was further validated ex vivo by using immunofluorescence microscopy of rhodamine and immunohistochemistry of APCs using anti-HLA-DR and anti-CD11b antibodies (Fig 4).

Group C: Conventional TACE with Bicarbonate Normalizes Tumor Acidosis and Restores Local Immune Cell Infiltration

Extracellular pH mapping of untreated VX2 liver tumors revealed tumor acidosis (mean extracellular pH, 6.78 ± 0.09; median, 6.77; range, 6.66–6.9) compared with liver parenchyma (mean extracellular pH, 7.18 ± 0.03; median, 7.19; range, 7.14–7.22) (P = .008). Tumor edge extracellular pH (mean, 6.88 ± 0.08; median, 6.89; range, 6.76–6.96) was slightly higher than whole tumor extracellular pH (P = .15). Although tumor extracellular pH remained almost unchanged after conventional TACE (mean, 6.85 ± 0.04; median, 6.84; range, 6.8–6.91; P = .19), the addition of bicarbonate to conventional TACE achieved an increase toward normalization of extracellular pH in the whole tumor (mean, 6.96 ± 0.05; median, 6.97; range, 6.90–7.01; P = .02 compared with baseline, P = .03 compared with 1 day after conventional TACE) and tumor edge (mean, 7.02 ± 0.04; median, 7.02; range, 6.98–7.05; P = .02 compared with baseline, P = .18 compared with 1 day after conventional TACE). We observed no differences in liver extracellular pH among all groups (conventional TACE: mean extracellular pH, 7.18 ± 0.04, median, 7.19, range, 7.11–7.22; conventional TACE with bicarbonate: mean extracellular pH, 7.14 ± 0.02, median, 7.15, range, 7.11–7.16; P = .14). Immunohistochemistry staining of APCs revealed expression primarily in the peritumoral rim of control tumors. Although we detected only a few HLA-DR– positive immune cells in the peritumoral rim after conventional TACE alone, conventional TACE with bicarbonate restored immune cell infiltration into the tumor micro-environment compared with untreated VX2 tumors (P = .002) and conventional TACE alone (P < .001) (Fig 5).

Discussion

Our study introduces molecular imaging techniques to reveal resistance mechanisms mediated by the immuno-metabolic interplay in the tumor micro-environment for strategic targeting of local-regional and immunotherapy in liver cancer. Immune cell–specific gadolinium 160–labeled antibodies and superparamagnetic iron oxide nanoparticles visualized on MRI scans in vivo showed curvilinear peritumoral distribution, corresponding to antigen-presenting cells and iron deposits in macrophages, respectively, at histopathologic examination. Although MR spectroscopy revealed acidosis of untreated VX2 rabbit liver tumors (mean pH, 6.78 ± 0.09) compared with liver parenchyma (mean pH, 7.18 ± 0.03) (P = .008), the combination of transarterial chemoembolization with bicarbonate achieved normalization of tumor pH (mean, 6.96 ± 0.05; P = .02) followed by increasing peritumoral immune infiltration (P = .002), thereby proving the link between the inherently acidic tumor micro-environment and immune cell dysfunction.

Overall, inflamed tumors, commonly referred to as “hot tumors,” are thought to be more susceptible to immunomodulatory treatment as compared with “cold” tumors without significant immune cell infiltration (24,25). Therefore, our cell-specific imaging tools can potentially be used to noninvasively evaluate susceptibility to immuno-oncologic therapies and help differentiate between actual tumor progression and atypical response patterns after immunotherapy, such as pseudoprogression caused by immune cell infiltration into the tumor micro-environment (26).

Chronic liver diseases are hypothesized to cause an imbalance in favor of immunotolerant signals to generate a proinflammatory milieu allowing for hepatic tumor formation and progression (27,28). Given this ineffective immunosurveillance, HCC seems to be a good candidate for immunotherapies aiming to restore anticancer immunity. However, the implementation of antigen-based immunotherapies has proven difficult given the complex adaptive nature of HCC and its immune-suppressive tumor micro-environment (27). Previously, oral bicarbonate increased the response to checkpoint inhibitors, leading to complete response when combined with adoptive T-cell therapy in murine models (29). Our findings further provide a strategy to exploit intra-arterial therapies as conditioning tools to convert immune-resistant tumor habitats toward a more susceptible tumor micro-environment. With increasing evidence supporting the importance of hydrophobicity in immune system activation, ethiodized oil–based conventional TACE may be a favorable modality for this endeavor (30).

Several imaging methods are in development that capture clinically relevant elements of the immune system, including radioactive tracers with relatively low focal resolution or targeting indirect immunogenic markers, such as programmed cell death protein 1 (31). SPIONs circulate in the blood, where they are phagocytosed by macrophages that migrate to areas of active inflammation. Although already approved by the U.S. Food and Drug Administration for the diagnosis of hepatic tumors, SPIONs may also be used for their combined therapeutic and diagnostic potential when incorporated into a complex with carriers (eg, small interfering RNA) that target molecules such as PD-L1 (20,32).

In addition to SPIONs, we developed a ^{160}Gd-conjugated immune tracer using anti–HLA-DR antibodies for the molecular analysis of the tumor immune landscape in the VX2 rabbit liver tumor model. Although VX2 tumors are of nonhepatic origin, they develop in immunocompetent hosts and their growth pattern and hyperglycolytic and neo-angiogenic profiles resemble the features of human HCC (16). A number of gadolinium-based contrast agents are available for clinical use and have proven safe, including gadoterate, which also contains ^{160}Gd used for the labeling in our study (33). We conjugated ^{160}Gd to anti–HLA-DR antibodies that bind peritumorally infiltrating APCs. Increased abundance of HLA-DR on the surface of APCs may occur in response to stimulation, and, thus, HLA-DR can also serve as a marker for immune stimulation (13). Although the conjugated antibody probes were injected in a selective fashion, this route of administration may be preferable for theranostic purposes by using antigen-specific therapeutics with increased local doses that could simultaneously be visualized in real time.

We had to overcome inherent limitations of small-animal tumor models and mimic the common clinical scenario. To do this, we used a human-size 3-T MRI with widely applicable imaging sequences to apply and validate the developed imaging tools in the rabbit liver tumor model. One limitation of our study was the spatial resolution of the voxels for MR spectroscopy, which could be improved by increasing the signal-to-noise-ratio with the use of a more sensitive coil. With regard to signal intensity quantification, future studies should include relaxometry to measure signal alterations caused by the experimental contrast agents. Last, statistics and generalizability of this study may be limited by its small sample size.

In conclusion, our translational study introduces noninvasive MRI-based markers for molecular tumor phenotyping that advances targeted approaches to disrupt resistance mechanisms hampering the efficacy of immuno-oncologic therapies. If implemented, the complementary imaging end points will help tailor personalized treatment regimens using immunotherapies alone and in combination with transarterial chemoembolization, to further explore the modulation of tumor acidity as a strategy to restore immune permissiveness in liver cancer.

Supplementary Material

Refer to Web version on PubMed Central for supplementary material.

Acknowledgment:

We thank Maolin Qui, PhD, for his advice and support regarding the quantitative MRI analysis.

This study was funded by the National Institutes of Health (R01 CA206180) and the Society of Interventional Oncology (19-001324). Research reported in this publication was also supported by the Yale CyTOF Facility and the Yale Liver Center Microscopy Core of the National Institute of Diabetes and Digestive and Kidney Diseases under award number P30 KD034989. F.H. and D.C. report grants from the National Institutes of Health (R01 EB023366). R.R.M. reports grants from the National Institutes of Health (U19 AI 089992).

Abbreviations

APC	antigen-presenting immune cell
HCC	hepatocellular carcinoma
HLA-DR	human leukocyte antigen–DR isotope
IMC	imaging mass cytometry
SPION	superparamagnetic iron oxide nanoparticle
TACE	transarterial chemoembolization
TmDOTP[52]	thulium (III) 1,4,7,10-tetraazacyclododecane-1,4,7,10-tetra

References

1. Bray F, Ferlay J, Soerjomataram I, Siegel RL, Torre LA, Jemal A. Global cancer statistics 2018: GLOBOCAN estimates of incidence and mortality worldwide for 36 cancers in 185 countries. CA Cancer J Clin 2018;68(6):394–424. [PubMed: 30207593]
2. Lencioni R, de Baere T, Soulen MC, Rilling WS, Geschwind JF. Lipiodol transarterial chemoembolization for hepatocellular carcinoma: A systematic review of efficacy and safety data. Hepatology 2016;64(1):106–116. [PubMed: 26765068]
3. Lencioni R, Kudo M, Ye SL, et al. GIDEON (Global Investigation of therapeutic DEcisions in hepatocellular carcinoma and Of its treatment with sorafeNib): second interim analysis. Int J Clin Pract 2014;68(5):609–617. [PubMed: 24283303]
4. Marquardt JU, Saborowski A, Czauderna C, Vogel A. The Changing Landscape of Systemic Treatment of Advanced Hepatocellular Carcinoma: New Targeted Agents and Immunotherapies. Target Oncol 2019;14(2):115–123. [PubMed: 30805831]
5. El-Khoueiry AB, Sangro B, Yau T, et al. Nivolumab in patients with advanced hepatocellular carcinoma (CheckMate 040): an open-label, non-comparative, phase 1/2 dose escalation and expansion trial. Lancet 2017;389(10088): 2492–2502. [PubMed: 28434648]
6. Calcinotto A, Filipazzi P, Grioni M, et al. Modulation of microenvironment acidity reverses anergy in human and murine tumor-infiltrating T lymphocytes. Cancer Res 2012;72(11):2746–2756. [PubMed: 22593198]
7. Turbitt WJ, Demark-Wahnefried W, Peterson CM, Norian LA. Targeting Glucose Metabolism to Enhance Immunotherapy: Emerging Evidence on Intermittent Fasting and Calorie Restriction Mimetics. Front Immunol 2019;10:1402. [PubMed: 31293576]
8. Ho PC, Kaech SM. Reenergizing T cell anti-tumor immunity by harnessing immunometabolic checkpoints and machineries. Curr Opin Immunol 2017;46:38–44. [PubMed: 28458087]
9. Buck MD, Sowell RT, Kaech SM, Pearce EL. Metabolic Instruction of Immunity. Cell 2017;169(4):570–586. [PubMed: 28475890]
10. Warburg O On respiratory impairment in cancer cells. Science 1956;124(3215):269–270. [PubMed: 13351639]
11. Huber V, Camisaschi C, Berzi A, et al. Cancer acidity: An ultimate frontier of tumor immune escape and a novel target of immunomodulation. Semin Cancer Biol 2017;43:74–89 10.1016/j.semcancer.2017.03.001. [PubMed: 28267587]
12. Mizukoshi E, Yamashita T, Arai K, et al. Enhancement of tumor-associated antigen-specific T cell responses by radiofrequency ablation of hepatocellular carcinoma. Hepatology 2013;57(4):1448–1457. [PubMed: 23174905]
13. Kambayashi T, Laufer TM. Atypical MHC class II-expressing antigen-presenting cells: can anything replace a dendritic cell? Nat Rev Immunol 2014;14(11):719–730 10.1038/nri3754. [PubMed: 25324123]
14. Savic LJ, Schobert IT, Peters D, et al. Molecular Imaging of Extracellular Tumor pH to Reveal Effects of Locoregional Therapy on Liver Cancer Microenvironment. Clin Cancer Res 2020;26(2):428–438. [PubMed: 31582517]
15. Lee HL, Jang JW, Lee SW, et al. Inflammatory cytokines and change of Th1/Th2 balance as prognostic indicators for hepatocellular carcinoma in patients treated with transarterial chemoembolization. Sci Rep 2019;9(1):3260. [PubMed: 30824840]
16. van Breugel JMM, Geschwind JF, Mirpour S, et al. Theranostic application of lipiodol for transarterial chemoembolization in a VX2 rabbit liver tumor model. Theranostics 2019;9(13):3674–3686. [PubMed: 31281506]
17. Coman D, Peters DC, Walsh JJ, et al. Extracellular pH mapping of liver cancer on a clinical 3T MRI scanner. Magn Reson Med 2020;83(5):1553–1564. [PubMed: 31691371]
18. Giesen C, Wang HA, Schapiro D, et al. Highly multiplexed imaging of tumor tissues with subcellular resolution by mass cytometry. Nat Methods 2014;11(4):417–422. [PubMed: 24584193]
19. Ahmed M, Kumar G, Gourevitch S, et al. Radiofrequency ablation (RFA)-induced systemic tumor growth can be reduced by suppression of resultant heat shock proteins. Int J Hyperthermia 2018;34(7):934–942. [PubMed: 29631466]

20. Iv M, Samghabadi P, Holdsworth S, et al. Quantification of Macrophages in High-Grade Gliomas by Using Ferumoxytol-enhanced MRI: A Pilot Study. Radiology 2019;290(1):198–206. [PubMed: 30398435]
21. Jones HW. The Distribution of Inorganic Iron in Plant and Animal Tissues. Biochem J 1920;14(5):654–659. [PubMed: 16742921]
22. Nair A, Morsy MA, Jacob S. Dose translation between laboratory animals and human in preclinical and clinical phases of drug development. Drug Dev Res 2018;79(8):373–382. [PubMed: 30343496]
23. Gandon Y, Olivié D, Guyader D, et al. Non-invasive assessment of hepatic iron stores by MRI. Lancet 2004;363(9406):357–362. [PubMed: 15070565]
24. van der Woude LL, Gorris MAJ, Halilovic A, Figdor CG, de Vries IJM. Migrating into the Tumor: a Roadmap for T Cells. Trends Cancer 2017;3(11):797–808. [PubMed: 29120755]
25. Gajewski TF, Corrales L, Williams J, Horton B, Sivan A, Spranger S. Cancer Immunotherapy Targets Based on Understanding the T Cell-Inflamed Versus Non-T Cell-Inflamed Tumor Microenvironment. Adv Exp Med Biol 2017;1036:19–31. [PubMed: 29275462]
26. Onesti CE, Frères P, Jerusalem G. Atypical patterns of response to immune checkpoint inhibitors: interpreting pseudoprogression and hyperprogression in decision making for patients' treatment. J Thorac Dis 2019;11(1):35–38. [PubMed: 30863564]
27. Roth GS, Decaens T. Liver immunotolerance and hepatocellular carcinoma: Patho-physiological mechanisms and therapeutic perspectives. Eur J Cancer 2017;87:101–112. [PubMed: 29145036]
28. Tomaszewski W, Sanchez-Perez L, Gajewski TF, Sampson JH. Brain Tumor Microenvironment and Host State: Implications for Immunotherapy. Clin Cancer Res 2019;25(14):4202–4210. [PubMed: 30804019]
29. Pilon-Thomas S, Kodumudi KN, El-Kenawi AE, et al. Neutralization of Tumor Acidity Improves Antitumor Responses to Immunotherapy. Cancer Res 2016;76(6):1381–1390 [Published correction appears in Cancer Res 2017;77(9):2552.]. [PubMed: 26719539]
30. Moyano DF, Goldsmith M, Solfiell DJ, et al. Nanoparticle hydrophobicity dictates immune response. J Am Chem Soc 2012;134(9):3965–3967. [PubMed: 22339432]
31. Ehlerding EB, England CG, McNeel DG, Cai W. Molecular Imaging of Immunotherapy Targets in Cancer. J Nucl Med 2016;57(10):1487–1492. [PubMed: 27469363]
32. Luo X, Peng X, Hou J, Wu S, Shen J, Wang L. Folic acid-functionalized polyethylenimine superparamagnetic iron oxide nanoparticles as theranostic agents for magnetic resonance imaging and PD-L1 siRNA delivery for gastric cancer. Int J Nanomedicine 2017;12:5331–5343. [PubMed: 28794626]
33. Hope TA, Doherty A, Fu Y, Aslam R, Qayyum A, Brasch RC. Gadolinium accumulation and fibrosis in the liver after administration of gadoxetate disodium in a rat model of active hepatic fibrosis. Radiology 2012;264(2):423–427. [PubMed: 22570507]
34. Carvajal-Hausdorf DE, Patsenker J, Stanton KP, et al. Multiplexed (18-Plex) Measurement of Signaling Targets and Cytotoxic T Cells in Trastu-zumab-Treated Patients using Imaging Mass Cytometry. Clin Cancer Res 2019;25(10):3054–3062. [PubMed: 30796036]
35. Chapiro J, Sur S, Savic LJ, et al. Systemic delivery of microencapsulated 3-bromopyruvate for the therapy of pancreatic cancer. Clin Cancer Res 2014;20(24):6406–6417. [PubMed: 25326230]

Key Results

- Immune cell–specific gadolinium 160–labeled antibodies and superparamagnetic iron oxide nanoparticles visualized on MRI scans showed curvilinear peritumoral distribution, corresponding to antigen-presenting cells and iron deposits in macrophages, respectively.
- Extracellular pH–specific MR spectroscopy of untreated VX2 rabbit liver tumors revealed acidosis (mean extracellular pH, 6.78 ± 0.09) compared with liver parenchyma (mean extracellular pH, 7.18 ± 0.03) ($P = .008$) and peritumoral immune cell exclusion.
- Normalization of tumor pH (mean, 6.96 ± 0.05; $P = .02$) by using bicarbonate during transarterial chemoembolization increased peri- and intratumoral immune cell infiltration compared with untreated tumors ($P = .002$).

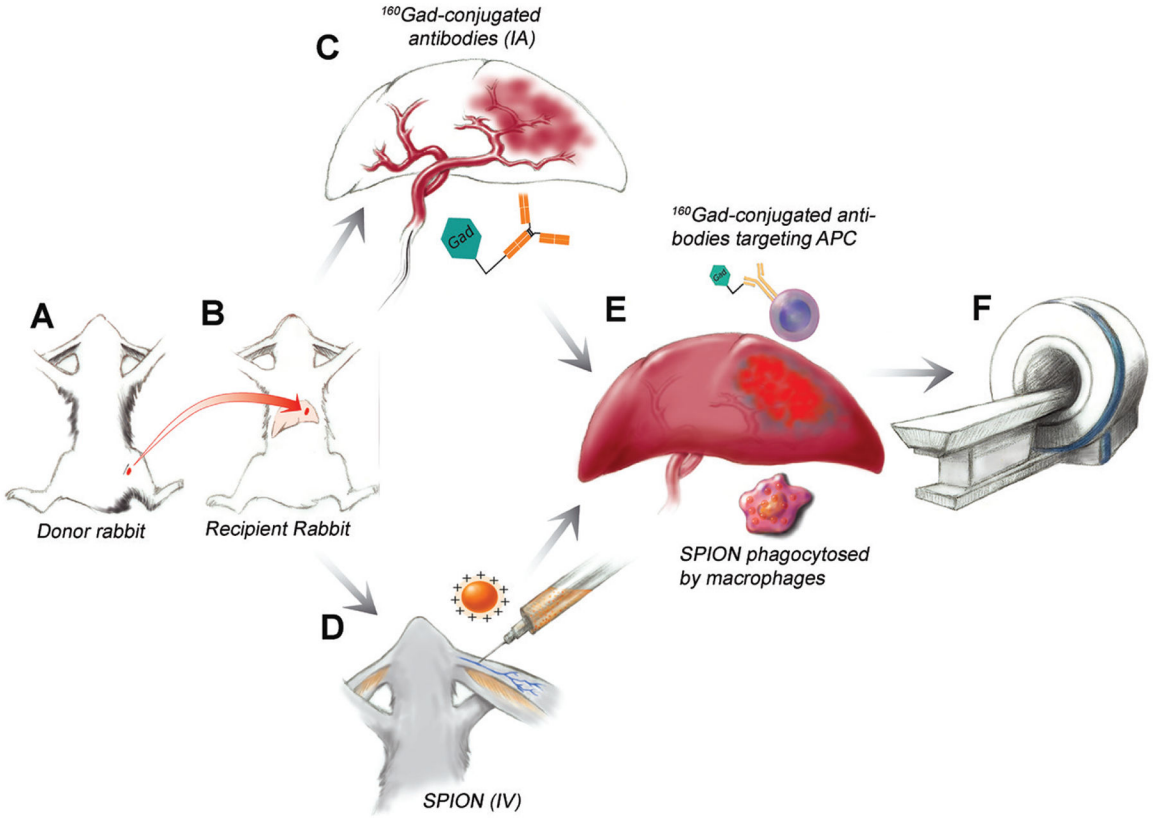

Figure 1:

Diagram illustrates the experimental design of immune cell imaging in vivo. *A*, VX2 liver tumor chunks were injected into the hind leg of a donor rabbit. *B*, Tumor chunks were harvested and injected into the left liver of the recipient rabbit and allowed to grow for 14 days. *C*, Three rabbits received intra-arterial (IA) injections of gadolinium 160 (^{160}Gd)–labeled anti–human leukocyte antigen–DR isotope antibodies and, *D*, three were intravenously (IV) injected with superparamagnetic iron oxide nanoparticles (SPION). *E*, ^{160}Gd-conjugated antibodies target antigen-presenting immune cells (APC) in the peritumoral rim and SPIONs are phagocytosed by peritumoral macrophages. *F*, MRI was performed and imaging findings were confirmed with radiologic-pathologic correlation.

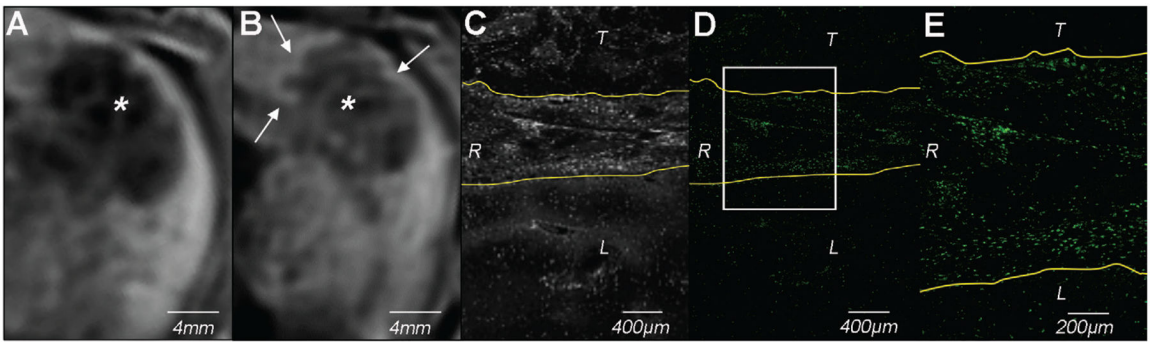

Figure 2:

In vivo molecular imaging of peritumoral antigen-presenting immune cell infiltrate using gadolinium 160 (^{160}Gd)–labeled anti–human leukocyte antigen–DR isotope (HLA-DR) antibodies. *A*, Baseline T1-weighted axial MRI scan of VX2 liver tumor (∗). *B*, Peritumoral rim enhancement (arrows) on T1-weighted axial Dixon MRI scan (repetition time, 5.19 msec; echo times, 2.46 and 3.69 msec) obtained 24 hours after intra-arterial administration of ^{160}Gd-labeled anti–HLA-DR antibody indicates peritumoral immune cell infiltrate. * = tumor. *C*, Bright field image and, *D, E*, colored images from ex vivo imaging mass cytometry of tissue harvested from the rabbit in *A* and *B* after ablation of ^{160}Gd (^{160}Gd in green) confirm deposition of ^{160}Gd-labeled anti–HLA-DR antibody in the peritumoral rim. The box in *D* indicates the the area of magnification for *E*. L = liver, R = peritumoral rim, T = tumor.

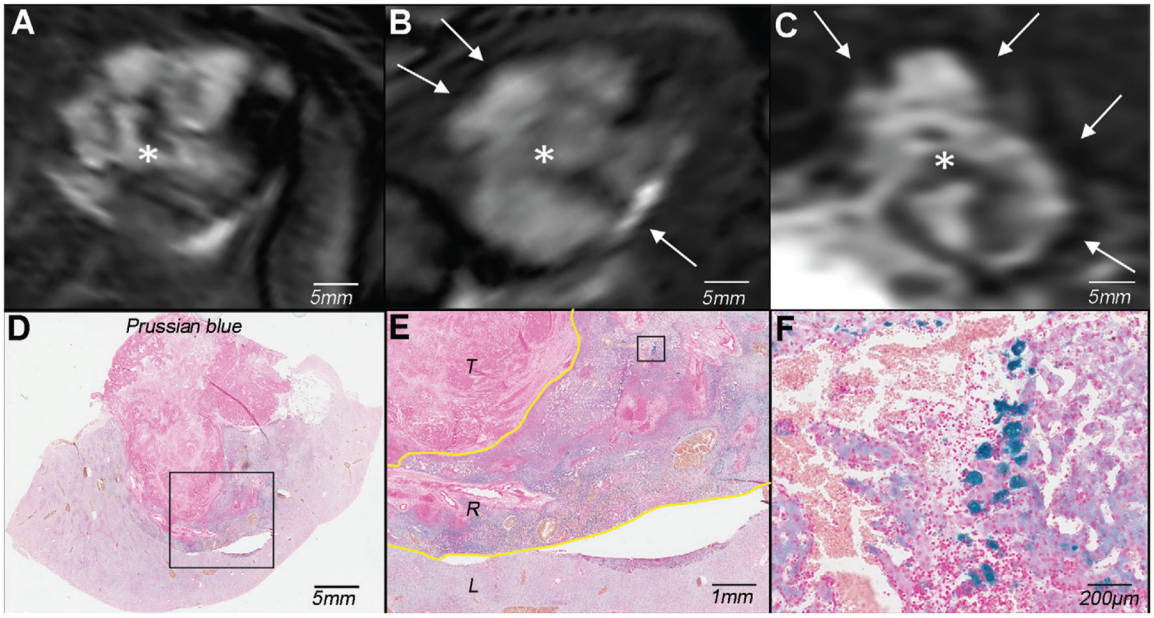

Figure 3:

In vivo molecular imaging of superparamagnetic iron oxide nanoparticles (SPIONs) reveals macrophage infiltration in the peritumoral rim. *A*, Baseline T2-weighted fat-suppressed axial spin-echo MRI scan (repetition time msec/echo time msec, 1000/78) of VX2 liver tumor (*). *B*, T2-weighted axial and, *C*, coronal MRI scans obtained 24 hours after SPION administration show hypointense peritumoral rim (arrows) indicative of peritumoral retention of iron. * = tumor. *D–F*, Photomicrographs of iron (Prussian blue stain) reveal deposition of SPIONs primarily in the peritumoral rim at, *D*, 31 and, *E*, 35 magnification after phagocytosis by macrophages as seen at, *F*, 320 magnification. The boxes in *D* and *E* indicate areas of magnification for *E* and *F*, respectively. The yellow lines in *E* outline the peritumoral rim. L = liver, R = peritumoral rim, T = tumor.

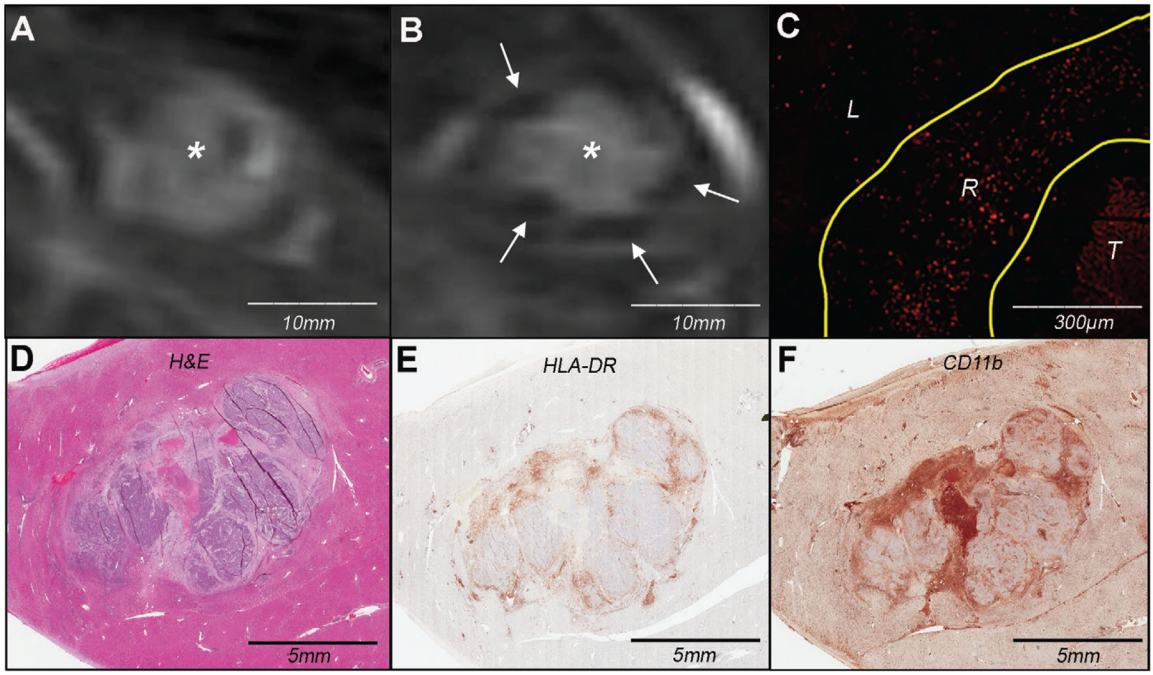

Figure 4:

Molecular imaging of cellular uptake of rhodamine-conjugated superparamagnetic iron oxide nanoparticles (SPIONs) in peritumoral macrophages. *A*, Baseline T2-weighted fat-suppressed axial spin-echo MRI scan (repetition time msec/echo time msec, 1000/78) of VX2 liver tumor (*). *B*, Hypointense peritumoral rim demarcation (arrows) on T2-weighted axial MRI scan obtained 24 hours after administration of rhodamine-conjugated SPIONs indicates peritumoral retention. * = tumor. *C*, Immunofluorescence image of rhodamine on tissue harvested from the same rabbit confirms deposition of SPIONs in the peritumoral rim (outlined by yellow lines). L = liver, R = peritumoral rim, T = tumor. *D*, Photomicrograph (hematoxylin-eosin [H&E] stain) of VX2 tumor and surrounding liver. *E*, *F*, Immunohistochemistry with, *E*, anti–human leukocyte antigen–DR isotope (HLA-DR) and, *F*, anti-CD11b antibodies reveals antigen-presenting immune cells and macrophages in the peritumoral rim, respectively.

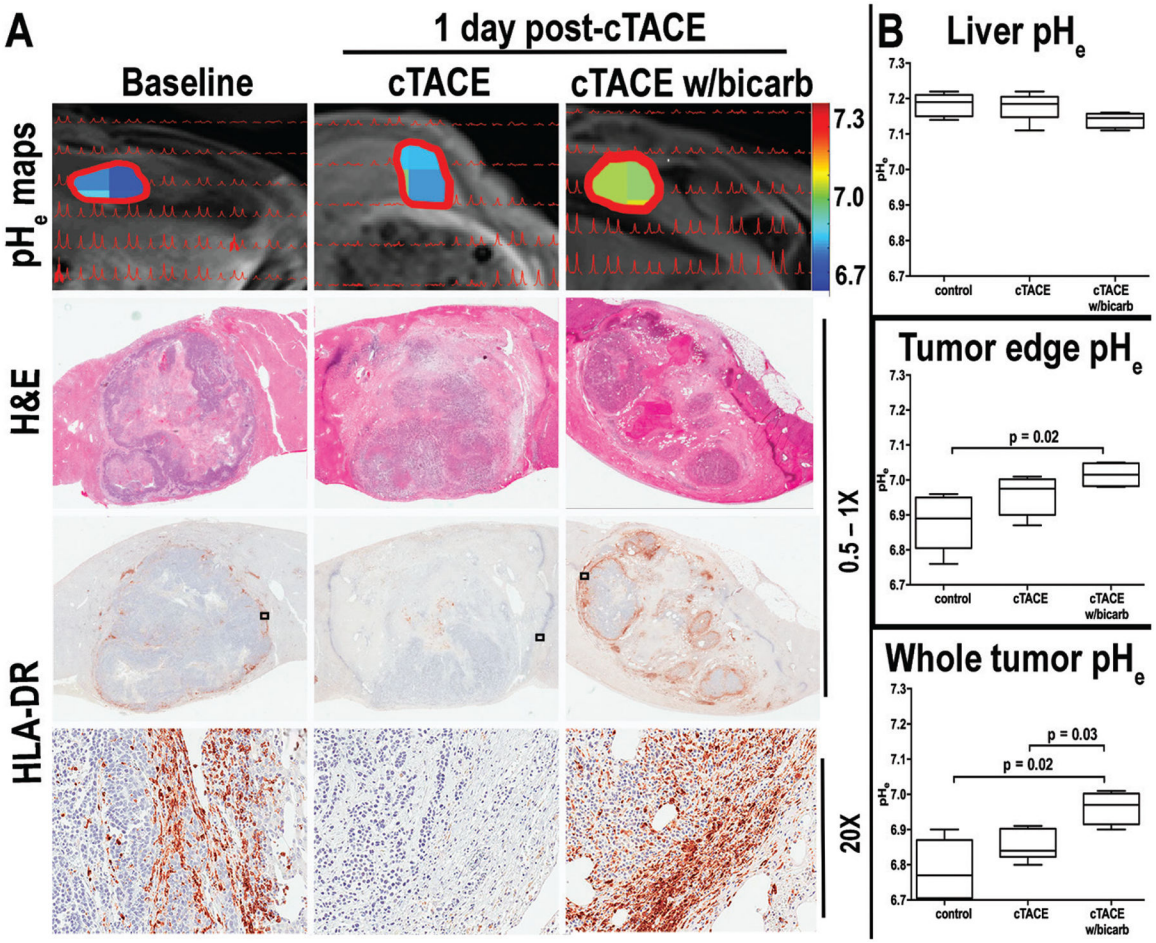

Figure 5:

A, Images demonstrate that normalization of extracellular tumor pH (pH_e) neutralizes inherent tumor acidosis and restores immune permissiveness after conventional transarterial chemoembolization (TACE) (cTACE). Top, peaks from extracellular pH spectroscopy are shown in red, overlaid on the corresponding anatomic T1-weighted axial MRI scans (repetition time msec/echo time msec, 5.2/2.5). Color map overlays illustrate extracellular tumor pH. Middle, Hematoxylin-eosin (H&E) and, bottom, human leukocyte antigen–DR isotope (HLA-DR) receptor staining reveals peritumoral immune cell infiltration in acidic untreated tumors. While extracellular tumor pH changes after conventional TACE remained insignificant and immune cell infiltrates were similar to or decreased compared with untreated tumors, conventional TACE with bicarbonate (cTACE w/bicarb) significantly increased extracellular pH of the tumor and tumor edge, boosting peritumoral immune cell infiltration. *B*, Box-and-whisker plots indicate extracellular (pH_e) differences in control rabbits and those treated with conventional TACE (cTACE) and conventional TACE with bicarbonate (cTACE w/bicarb). Data are medians (lines in boxes) and 25th to 75th percentiles (bottom and top of boxes) and ranges (whiskers) (Mann-Whitney *U*, Kruskal-Wallis test).